

# Causal Effect of Leading-Edge Sawtooth Configuration on Flow Field Characteristics and Aerodynamic Losses in the Supersonic Compressor Cascade

S. J. Hu, Z. J. Wei<sup>†</sup>, M. Ni and G. M. Ren

*Shenzhen Key Laboratory of Wide-Speed-Range and Variable-Density Continuous Wind Tunnel, Southern University of Science and Technology, Shenzhen 518055, China*

*Department of Mechanics and Aerospace Engineering, College of Engineering, Southern University of Science and Technology, Shenzhen 518005, China*

<sup>†</sup>Corresponding Author Email: [weizj@sustech.edu.cn](mailto:weizj@sustech.edu.cn)

## ABSTRACT

This study focuses on the TM-141 supersonic compressor blade as the subject of investigation. Utilizing the Reynolds-averaged numerical simulation approach, the study examines the impact of the leading-edge sawtooth structure on the blade grid, flow field characteristics, and flow losses. Comparative analysis is conducted between numerical results and experimental data to assess the influence of the leading-edge sawtooth structure under various conditions, including fixed Mach numbers and variable static pressure ratios, fixed static pressure ratios and variable Mach numbers, and fixed Mach numbers and fixed static pressure ratios. The findings reveal that the leading-edge sawtooth structure effectively alters the distribution of total pressure loss coefficients within the blade grid channels, mitigates leading-edge spikes, and improves trailing-edge blade morphology, consequently reducing trailing-edge losses and total pressure loss compared to benchmark blade grids. These results offer insights for mitigating losses and enhancing efficiency in the transonic region of compressor blade operation, thereby providing a foundation for further investigation into the effects of leading-edge sawtooth structures on flow fields.

## Article History

*Received February 28, 2024*

*Revised June 8, 2024*

*Accepted July 4, 2024*

*Available online October 2, 2024*

## Keywords:

*Leading-edge Sawtooth*

*Transonic compressor cascade*

*Cascade characteristics*

*Aerodynamic*

*Shock wave /boundary layer interaction*

## 1. INTRODUCTION

The evolution of aero-engine technology has consistently pursued goals of enhanced thrust-to-weight ratio, reduced fuel consumption, and extended service life. The critical aero-engine component to realize this performance improvement is the compressor, whose robust compressive capabilities are imperative for achieving high thrust-to-weight ratios. As the compression ratio within the compressor stages increases, the operational load also increases. Consequently, with the ongoing advancements, the compressor's performance requirements are becoming increasingly stringent.

Sawtooth structures have been proven to be quite effective in diminishing both aerodynamic noise and flow loss, leading to their widespread integration across various airfoils, rotor blades, and within the compressor's rotational and stationary components. These structures are strategically positioned and are typically distinguished into two categories: trailing-edge and leading-edge sawtooth configurations. [Liu et al. \(2022\)](#) implemented trailing-edge sawtooth structures to demonstrate that they can significantly attenuate the interaction noise between the

wings on tandem airfoils. Inspired by the owl wings, [Yang et al. \(2020a, b\)](#) used trailing-edge sawtooth structure for noise reduction in a multi-copter rotor. Aiming to diminish the noise generated by multi-aircraft rotors, the wave rotor design was optimized based on the foundational structure of a reference rotor (denoted as BL). This optimization involved a strategic adjustment, where alternating cross-sections were shifted toward the rotor's trailing edge to enhance the acoustic performance. [He et al. \(2019a, b\)](#) thoroughly investigated the impact of trailing-edge sawtooth structures on both noise and flow loss. The results revealed that these structures are effective in mitigating both velocity and total pressure losses at the trailing edge, consequently attenuating the associated noise. Notably, it has been widely established that the long sawtooth blades have better noise reduction and flow loss mitigation capabilities than the standard blade and shorter sawtooth variants. The above studies demonstrated that trailing-edge sawtooth structures can significantly reduce aerodynamic losses. Subsequently, several researchers have examined the underlying mechanisms for this loss reduction. For example, [Wang \(2019\)](#) took the high-load compressor cascade NACA0065-K48 blade as the research object and investigated the effect of tooth width, tooth height, and tooth arrangement of the trailing-edge

**NOMENCLATURE**

$\lambda$	sawtooth spanwise length	$c$	blade chord length
$s$	pitch length	$p_2/p_1$	static pressure ratio
$\xi$	total pressure loss coefficient	$L/D$	lift-drag ratio
$C_p$	static pressure coefficient	$D'_{spike}$	leading-edge spike evaluation factor

sawtooth structure on the blade performance and the flow field structure, and the loss mechanisms were also analyzed. Based on the Reynolds-averaged Navier-Stokes (RANS) numerical approach, Yu (2018) elucidated the role of trailing-edge sawtooth structures in enhancing the aerodynamic performance of high-speed diffuser grates. The findings revealed the intricate dynamics by which these structures facilitate passive flow control, contributing to a broader understanding of the aerodynamic design nuances (Yu 2018). Wu (2016) proposed a trailing-edge sawtooth blade based on the effect of the sawtooth flow vortex tube and the trailing shear layer on the main-stream suction to enhance the stability of the fan/pressure machine. Wang (2020) explored the impact of sawtooth distribution on the trailing edges of blades and static sub-trailings on the aerodynamic stability of high-speed axial-flow compressors. Zou et al. (2021) comprehensively analyzed the implications of modifying the static lobe's trailing-edge with a sawtooth structure in a 3.5-stage pressurized air compressor. Further, the effects of sawtooth shape and its position on the compressor's rotational speed characteristics were examined. Chen et al. (2017, 2018) demonstrated that sawtooth structures outperform their wider-teeth counterparts in overall aerodynamic performance. They highlighted that the efficacy of trailing-edge sawtooth structure in reducing trailing-edge losses is intricately linked to the blade's inlet angle of attack and the structure's role in vortex system development within the flow field. Thus, numerous studies on trailing-edge sawtooth structures have consistently demonstrated that such structures can significantly reduce both noise and flow loss.

Although trailing-edge sawtooth structures are widely used, several studies have also been conducted on leading-edge sawtooth structures. For example, Chen et al. (2016, 2021) demonstrated that leading-edge structures with large amplitudes and short wavelengths can significantly reduce aerodynamic noise. Further, nine sawtooth configurations were analyzed to show that these structures could potentially eliminate unstable noise within the laminar boundary layer, especially at higher amplitudes and shorter wavelengths. Moreover, it was found that sawtooth edges induced flow vortices, affecting downstream flow. Sun et al. (2021) analyzed the impact of pressure pulsations and the formation of separation vortices at various critical edge locations, specifically at the leading edge of the sawtooth structure as well as the leading and trailing edges of the blade, where the NACA0018 airfoil was utilized as the test object. Hu (2020) installed leading-edge sawtooth structures on unmanned aerial vehicles (UAVs) to demonstrate that incorporating such structures into UAV rotors can significantly attenuate the mid- to high-frequency broadband noise associated with the rotor's forward flight operations. Overall, it has been widely established that the leading-edge sawtooth structures can generate flow vortices to positively influence the flow dynamics at the downstream boundary layer. Moreover, this structural innovation can effectively limit the noise induced by boundary layer instabilities.

Until now, sawtooth structures have been extensively utilized, predominantly at the trailing edges of blades and rotors within subsonic compressors, to mitigate noise and flow loss. Although some researchers have examined the impact of leading-edge sawtooth structures on subsonic compressors, particularly pressure pulsations and vortex separation, the dynamic characteristics are markedly different under transonic conditions. In this case, the interaction between the excitation wave and the boundary layer can intensify the flow loss, posing a distinct set of challenges. The complex issues related to the reduction of flow loss in transonic flows as well as the comparative effects of leading-edge sawtooth structures on the interference caused by the interaction between excitation waves and boundary layer remain unclear and necessitate further investigation. To address the above issues, in this work, the JAXA's TM-141 supersonic compressor blade profile (Kondo et al., 1968) is considered as the object of study, which is a supersonic cascade. Taking the compressor blade as the baseline cascade, a triangular sawtooth structure is designed on its leading edge to investigate the supersonic transonic velocity flow with and without the sawtooth structure. Further, the flow field characteristics and aerodynamic losses of the transonic compressor cascade are examined, both in the presence and absence of sawtooth structure. The main objective of this study is to elucidate the effect of sawtooth configurations on the flow dynamics of such compressor cascades. Concurrently, effective strategies are established to minimize the losses within the mid-section of the pressure compressor blades, specifically in the transonic segment, thereby enhancing the efficiency and pressure ratio, which is crucial for boosting the practical engineering applications of such structures.

## 2. COMPUTATIONAL MODELS

### 2.1 Research Object and Computational Domain

JAXA's TM-141 lobe-type supersonic compressor was used as the object of study, and its detailed geometric and aerodynamic design parameters can be found in an earlier report (Kondo et al., 1968). The original blade type had a chord length of 30 mm, a grid pitch of 13.76 mm, a stagger angle of 50.5°, and a blade camber angle of 7.8°. The leaf blade was scaled up twice to obtain a blade chord length  $c$  of 60 mm, a pitch  $s$  of 27.52 mm, and a spreading height of 9 mm. A round leading edge was adopted in the leaf blade, whose thickness was 1.2 mm.

In this study, the effects of a leading-edge sawtooth configuration on the TM-141 compressor blade have been investigated, which is referred to as the baseline blade. The leading edge of the baseline blade was carefully engineered with a sawtooth profile, characterized by a tooth width of 3 mm and a tooth depth of 2.4 mm, resulting in the leading-edge sawtooth blade. Figure 1 illustrates a schematic of the leading-edge sawtooth blade. To save computational resources and streamline the meshing process, a tooth structure with a span of  $\lambda = 3$  mm

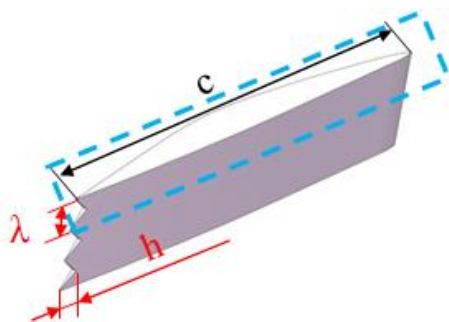


Fig. 1 Leading-edge sawtooth cascade model

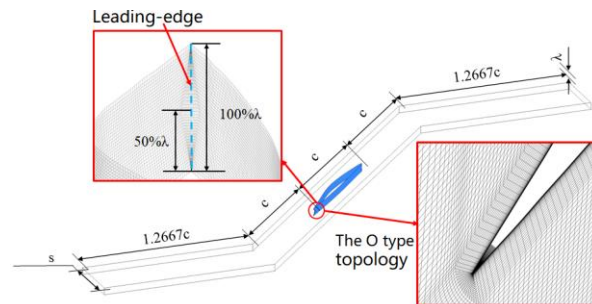


Fig. 2 Computational domain and leading-edge sawtooth cascade mesh

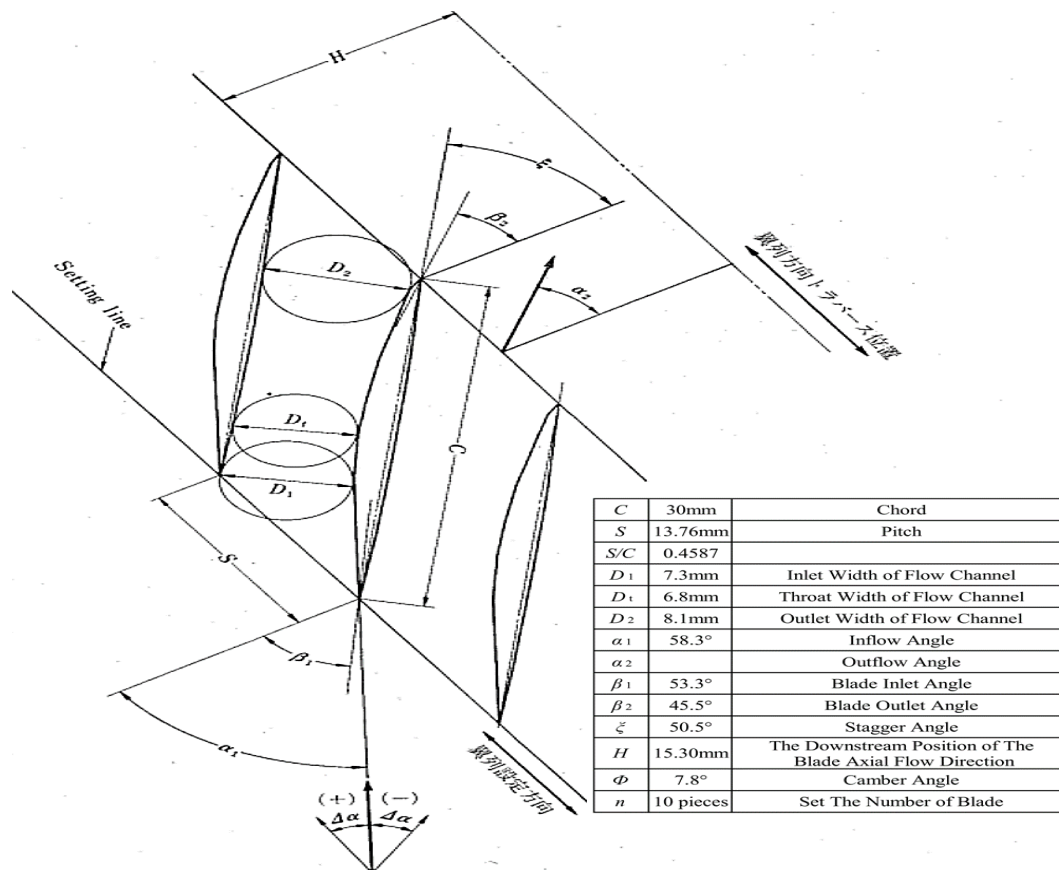


Fig. 3 Airfoil geometric parameters

is incorporated in the model, as marked by the blue dashed box in Fig. 1. Similarly, the computational domain encompassing the leading-edge sawtooth blade is illustrated in Fig. 2. Figure 3 displays the airfoil and its geometric parameters, Fig. 4 presents an enlarged view of the geometric parameters shown in Fig. 3, and Fig. 5 illustrates the airfoil data.

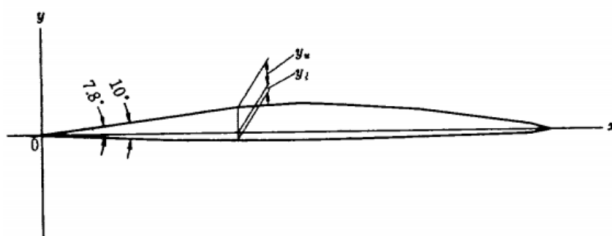
## 2.2 Computational Grid and Solution Setup

The computational mesh was generated by ANSYS ICEM software in which the H-O-H topology was adopted. Specifically, the mesh in the inlet domain, outlet domain, and mainstream channels, such as the blade channel, had H topology, while the mesh of the area around the blade had O topology, and the same topology was adopted in different cases. The O-type topology allows for better control over the spacing of the grid cells near the wall surface. This is important because the boundary layer, where the fluid interacts with the wall, is a critical region

for capturing the effects of viscosity and turbulence (Liang et al., 2021). Besides, H-type grids offer higher computational accuracy than the unstructured grids. Structured grids have relatively lower memory and CPU consumption. They are suitable for calculations involving viscous flows, especially when high resolution of boundary layer flows is required. Within the three-dimensional (3D) computational domain, a grid system comprising 1.13 million cells was utilized. To accurately capture the effects of the attached surface layer on the blade surface, the boundary layer grid density was calibrated to ensure an adequate resolution. Since the main aim of this study is to examine the impact of the sawtooth structure on the leading edge of the blade, particularly the leaf grating, the regions adjacent to the blade's wall surface and the leading-edge sawtooth structure were subjected to local mesh refinement. The first layer of the mesh adjacent to the blade wall was designed to have a height of 0.001 mm to achieve a dimensionless height ( $y^+$ ) of less than or

$C$	30mm	Chord
$S$	13.76mm	Pitch
$S/C$	0.4587	
$D_1$	7.3mm	Inlet Width of Flow Channel
$D_t$	6.8mm	Throat Width of Flow Channel
$D_2$	8.1mm	Outlet Width of Flow Channel
$\alpha_1$	58.3°	Inflow Angle
$\alpha_2$		Outflow Angle
$\beta_1$	53.3°	Blade Inlet Angle
$\beta_2$	45.5°	Blade Outlet Angle
$\zeta$	50.5°	Stagger Angle
$H$	15.30mm	The Downstream Position of The Blade Axial Flow Direction
$\Phi$	7.8°	Camber Angle
$n$	10 pieces	Set The Number of Blade

Fig. 4 Enlarged view of the relevant parameters



$x$	$y_u$	$y_l$	$x$	$y_u$	$y_l$
0.000	0.000	0.000	16.154	1.771	-0.340
1.154	0.158	-0.044	17.308	1.725	-0.328
2.308	0.316	-0.104	18.462	1.661	-0.311
3.462	0.474	-0.132	19.615	1.575	-0.294
4.615	0.632	-0.177	20.769	1.476	-0.276
5.769	0.790	-0.221	21.923	1.361	-0.259
6.923	0.948	-0.242	23.077	1.223	-0.242
8.078	1.106	-0.265	24.231	1.067	-0.225
9.231	1.264	-0.282	25.385	0.905	-0.207
10.385	1.420	-0.300	26.539	0.732	-0.190
11.538	1.540	-0.317	27.693	0.553	-0.173
12.692	1.650	-0.328	28.847	0.363	-0.155
13.846	1.736	-0.340	30.000	0.000	-0.000
15.000	1.776	-0.346			

Fig. 5 Airfoil data

equal to 1.0, optimizing the grid for turbulence modeling. Figure 2 provides a visual representation of the mesh detail at the leading-edge sawtooth region of the blade.

Numerical simulations were performed utilizing the ANSYS CFX software, employing the 3D RANS equations as the mathematical framework. The  $k-\omega$  shear stress transport (SST) model was used in the simulations, which is particularly advantageous for predicting flow separation along the blade and for accurately describing the wall pressure and shear stress distributions. The SST model has the potential to bolster the accuracy of quantitative forecasting for intricate turbulent flows,

especially those with robust adverse pressure gradients and instances of flow separation that are typically encountered in axial compressors. There is a commitment to undertaking more exhaustive research on the SST model with the objective of refining its proficiency in the simulation of turbomachinery (Menter et al., 2003; Yin et al., 2010). The convective and viscous terms were formulated in a quasi-second-order high-resolution scheme, targeting a convergence criterion with a maximum residual of  $1 \times 10^{-4}$  or lower. For boundary conditions, the inlet was defined as a velocity inlet, specifying the static pressure, temperature, turbulence intensity, and the axial, circumferential, and radial velocities of the incoming flow. Conversely, the outlet was designated as a pressure outlet, with the static pressure provided. Symmetric plane boundaries were employed for the hub and shroud regions of the blade grid, while the blade surface itself was modeled with adiabatic, no-slip, and smooth wall boundary conditions. Periodic boundaries were utilized in the computational domain of leading-edge sawtooth blade grid, allowing for translational extension along the blade height. The specific boundary conditions are listed in Table 1.

Table 1 Boundary conditions

Parameter	Value
Inlet static pressure	101.3 kPa
Inlet static temperature	256.504 K
Inlet axial speed	227.738 m/s
Inlet circumferential speed	368.739 m/s
Inlet radial speed	0 m/s
Inlet airflow angle	58.3°
Incoming turbulence	1%
Outlet static pressure	151.988 kPa

### 2.3 Grid-Independence Verification

To verify the reliability of the numerical simulations, the grid independence of the meshes within the blade-grid channel was analyzed. Figure 6 illustrates the relationship between the total pressure loss coefficient of the blade grid and the grid resolution. It can be seen that the total pressure loss coefficient initially increases with the rise in grid number from 50,000 to 300,000. As the number of grids further increases to 3,000,000, the coefficient declines and eventually stabilizes, with negligible variation between 1,100,000 and 3,000,000 grids. This indicates that grid independence is achieved within this range, which implies that further increase in the number of grids does not affect the results. Consequently, a grid count of 1,100,000 is adopted, which meets the criteria for grid independence and ensures the reliability of the computational results.

### 3. VALIDATION OF NUMERICAL RESULTS

The blades and boundary conditions used in this study are the same as those for JAXA's TM-141 (Kondo et al., 1968), and the TM-141 compressor blade is used to assess the ability of the numerical method to simulate the total pressure loss coefficient in the direction of the blade pitch. In both the experiments and numerical simulations, it is considered that the Mach number  $Ma = 1.3$  and the static pressure ratio  $p_2/p_1 = 1.5$ . Figure 7

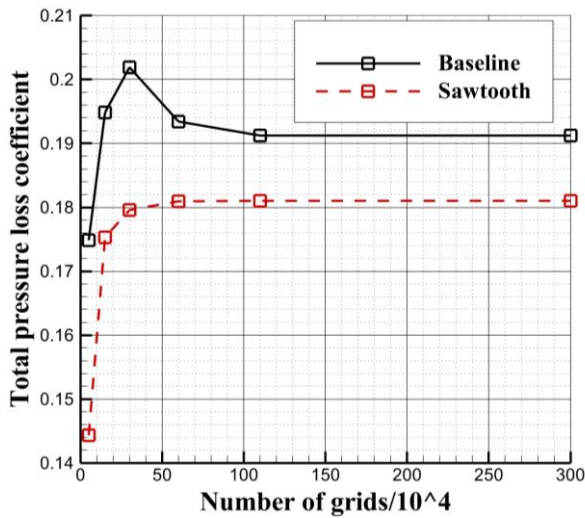


**Fig. 6** Variation in the total pressure loss coefficient with the number of blade grids

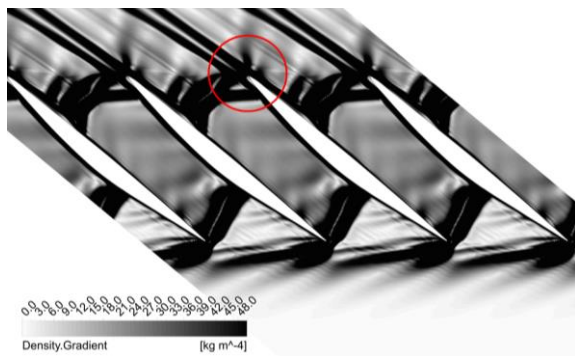


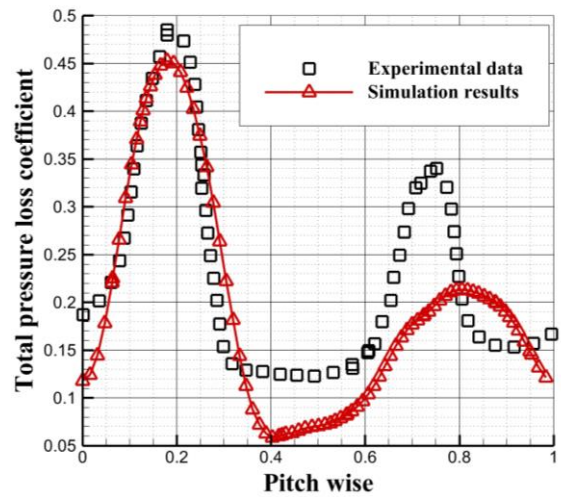
**Fig. 7** Channel density gradient cloud



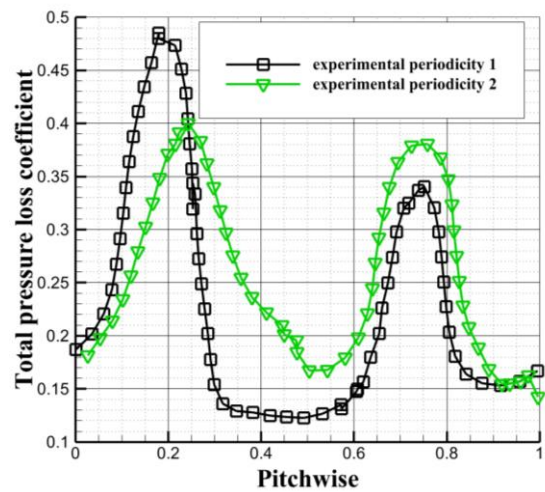
**Fig. 8** Experimental grain shadow map

and Fig. 8 show the numerically simulated density gradient cloud map and the experimental shadow maps, respectively. It is clear from these figures that the experimental and simulated flow field structures are consistent with each other.

Figure 9(a) compares the numerically simulated and experimentally measured distribution of the total pressure loss coefficient across grid spacing. Further, Fig. 9(b) compares the total pressure loss coefficient distributions from two distinct experimental cycles in the same spatial direction. Discrepancies between the simulated and experimental data are evident in the encircled region of Fig. 9(a). This divergence is further highlighted by the



(a) Comparison between the simulation and experimental results



(b) Adjacent blades within the same cascade under identical experimental conditions

**Fig. 9** Distribution of total pressure loss coefficients along the pitch direction of the baseline cascade

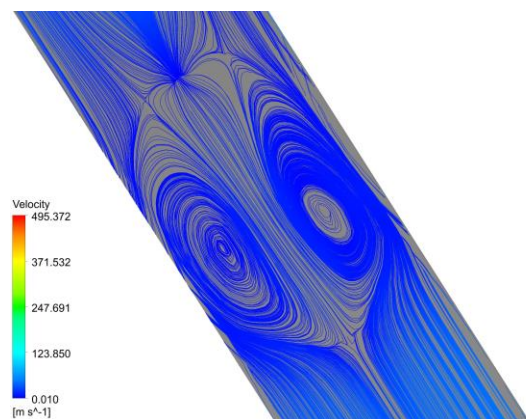


**Fig. 10** Wall flow spectrum of leading-edge sawtooth cascade with a span length of 3 mm

inconsistent experimental cycle in Fig. 9(b), potentially accounting for the discrepancies. Nonetheless, the simulation results, including the loss values at the trailing edge, are in good agreement with the experimental ones, which verifies the reliability of the numerical approach.

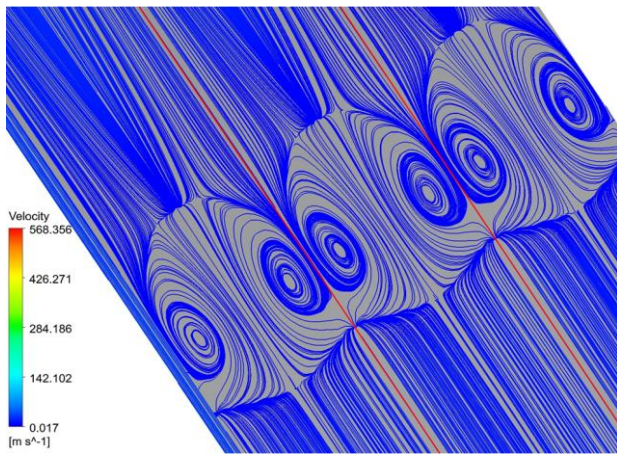


**Fig. 11** Wall flow spectrum of leading-edge sawtooth cascade with a span length of 3 mm

As mentioned before, the leading-edge sawtooth cascade is examined by using a span length of 3 mm. To verify the rationality of this span length, the results obtained under the span lengths of 9 mm (including three teeth) and 3 mm (including only one tooth) are compared. Figure 10 and Fig. 11 show the wall flow spectra of the leading-edge sawtooth cascades with span lengths of 3 and 9 mm, respectively. The red lines in Fig. 8 correspond to the same position as that shown for leading-edge sawtooth cascade with a span length of 3 mm. Comparing the red lines in Fig. 10 and Fig. 11, it is evident that the flow spectra are identical. Further, Fig. 12 reveals that the distribution of the total pressure loss coefficient along the pitch direction for the sawtooth cascades with span lengths of 3 and 9 mm are identical. The interference among the adjacent saw teeth is negligible. Consequently, employing a span length of 3 mm for the leading-edge sawtooth cascade and applying periodic boundary conditions to the upper and lower surfaces effectively conserves computational resources without compromising the simulation accuracy.

#### 4. CFD RESULTS AND DISCUSSION

##### 4.1 Effect of Static Pressure Ratio on the Performance of Leading-edge Sawtooth Cascade

###### (1) Variation in the Total Pressure Loss Coefficient

To compare the effects of the leading-edge sawtooth cascade and baseline cascade on the airflow dynamics, it is essential to examine how the total pressure loss coefficient for each cascade changes under various static pressure ratios. For an in-depth analysis, the range of static pressure ratio  $p_2/p_1$  is chosen to be 1.2-1.8. The corresponding total pressure loss coefficients of both types of cascade are depicted in Fig. 10. Here, we focus on the impact of the sawtooth structure on the flow field, specifically with respect to the baseline cascade, without dimensionalizing the turbocharging process. The total pressure loss coefficient serves as a metric for quantifying the overall pressure loss within the cascade, which can be expressed as follows:

$$\xi = \frac{P_{t,in} - P_{t,out}}{P_{t,in} - P_{s,in}} \quad (1)$$

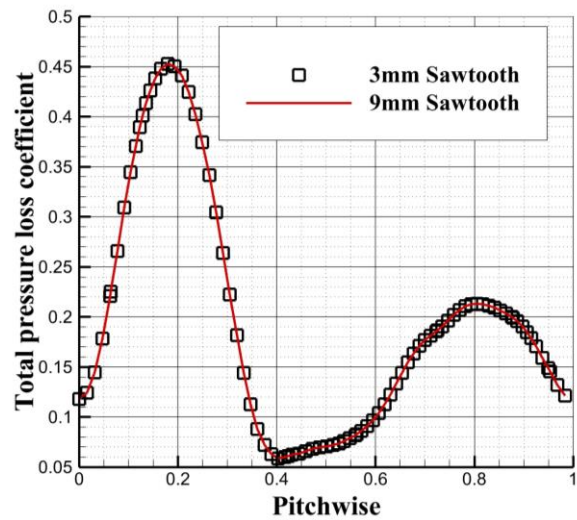


**Fig. 12** Comparison between the total pressure loss along the pitch direction between leading-edge sawtooth cascades with span lengths of 3 and 9 mm

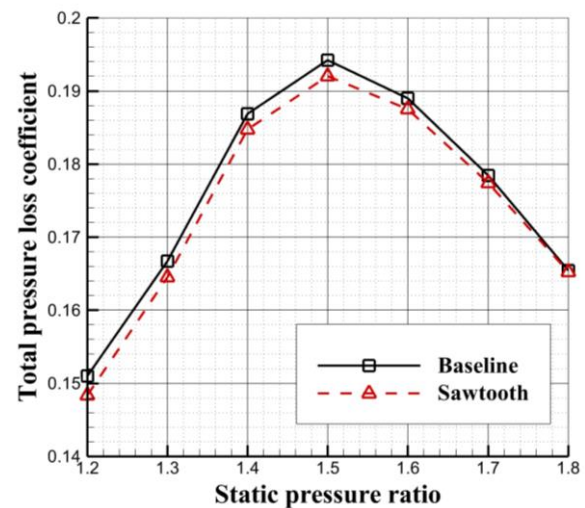


**Fig. 13** Variation in the total pressure loss coefficient with the static pressure ratio

where  $p_{t,in}$  is the absolute total pressure at the entrance of the cascade,  $p_{t,out}$  is the absolute total pressure at the outlet of the cascade, and  $p_{s,in}$  is the static pressure at the entrance of the cascade. The total pressure loss coefficient aspect with static pressure ratio is shown in Fig. 13.

To measure the extent of improvement or deterioration in the performance of the leading-edge sawtooth cascade with respect to that of the baseline cascade, the concept of the relative variation in the total pressure loss coefficient is utilized. This metric allows for a direct assessment of the optimization effects. This relative variation is expressed in Equation (2), and the corresponding data are presented in Fig. 14. The total pressure loss coefficients of the baseline cascade and the leading-edge sawtooth cascade, as well as the relative change rate of their total pressure loss coefficients with respect to the static pressure ratio, are depicted in Table 2.

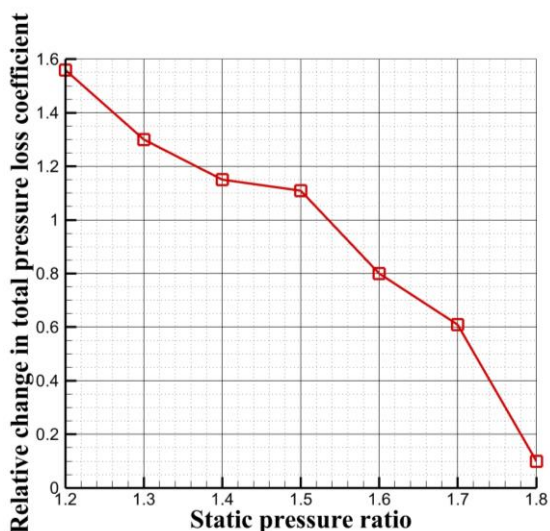


**Fig. 14** Relative variation in the total pressure loss coefficient with the static pressure ratio

$$\text{Relative variation} = \frac{\xi_1 - \xi_2}{\xi_1} \times 100\% \tag{2}$$

where  $\xi_1$  and  $\xi_2$  are the total pressure loss coefficients of the baseline cascade and leading-edge sawtooth cascade, respectively.

It can be seen in Fig. 13 that the average total pressure loss coefficient of the leading-edge sawtooth cascade is lower than that of the baseline cascade, suggesting that the introduction of sawtooth structure effectively minimizes the total pressure loss. As the static pressure ratio rises from 1.2 to 1.5, the total pressure loss coefficient increases, followed by a decline when the ratio further increases to 1.8. Additionally, Fig. 14 demonstrates that the relative change in the total pressure loss coefficient decreases with the increase in the static pressure ratio, indicating a stabilizing effect of the sawtooth structure across a broad range of pressure conditions. Integrating the trends observed in Fig. 13 and Fig. 14 with the data from Table 3,

**Table 2** The data about total pressure loss coefficient and relative change in total pressure loss coefficient with respect to static pressure ratio

Static pressure ratio	Baseling total pressure loss coefficient	Sawtooth total pressure loss coefficient	Relative change in total pressure loss coefficient
1.2	0.1510	0.1484	1.56%
1.3	0.1667	0.1646	1.3%
1.4	0.1869	0.1847	1.15%
1.5	0.1942	0.1920	1.11%
1.6	0.1890	0.1875	0.8%
1.7	0.1785	0.1774	0.61%
1.8	0.1654	0.1653	0.1%

**Table 3** The data about lift-drag ratio and relative change in lift-drag ratio with respect to static pressure ratio

Static pressure ratio	Baseling lift-drag ratio	Sawtooth lift-drag ratio	Relative change in lift-drag ratio
1.2	1.9406	1.9775	-1.9%
1.3	2.8934	2.9123	-0.65%
1.4	3.5828	3.6135	-0.86%
1.5	4.4439	4.4275	0.37%
1.6	5.6393	5.5630	1.35%
1.7	7.1951	7.0950	1.39%
1.8	9.2880	9.1028	1.99%

it is noted that at static pressure ratio  $p_2/p_1=1.2$ , the total pressure loss coefficient for the baseline cascade is 0.1510, whereas for the leading-edge sawtooth cascade, it is 0.1484, resulting in a relative change of 1.56%. At static pressure ratio  $p_2/p_1=1.3$ , the total pressure loss coefficient for the baseline cascade is 0.1667, and for the leading-edge sawtooth cascade, it is 0.1646, with a relative change of -1.3%. At static pressure ratio  $p_2/p_1=1.4$ , the total pressure loss coefficient for the baseline cascade is 0.1869, and for the leading-edge sawtooth cascade, it is 0.1847, leading to a relative change of 1.15%. When static pressure ratio  $p_2/p_1$  increases to 1.5, the total pressure loss coefficient for the baseline cascade is 0.1942, and for the leading-edge sawtooth cascade, it is 0.1920, with a minimal relative change of 1.11%. At static pressure ratio  $p_2/p_1=1.6$ , the total pressure loss coefficient for the baseline cascade is 0.1890, and for the leading-edge sawtooth cascade, it is 0.1875, corresponding to a relative change of 0.8%. At static pressure ratio  $p_2/p_1=1.7$ , the total pressure loss

coefficient for the baseline cascade is 0.1785, and for the leading-edge sawtooth cascade, it is 0.1774, with a relative change of 0.61%. Finally, at static pressure ratio  $p_2/p_1=1.8$ , the total pressure loss coefficient for the baseline cascade is 0.1654, and for the leading-edge sawtooth cascade, it is 0.1653, with a relative change of 0.1%. Regardless of the variation in the static pressure ratio, the total pressure loss coefficient of the leading-edge sawtooth cascade is consistently lower than that of the baseline cascade.

**(2) Variation in the Lift-Drag Ratio**

In this section, the influence of static pressure ratio on the lift-drag ratio is analyzed. The lift-drag ratios of baseline and leading-edge sawtooth cascades under different static pressure ratios are shown in Fig. 15. The relative change in the lift-drag ratio is used to quantify the improvement/deterioration in the lift-drag ratio of the leading-edge sawtooth cascade with respect to that of the baseline cascade. The relative change in the lift-drag ratio

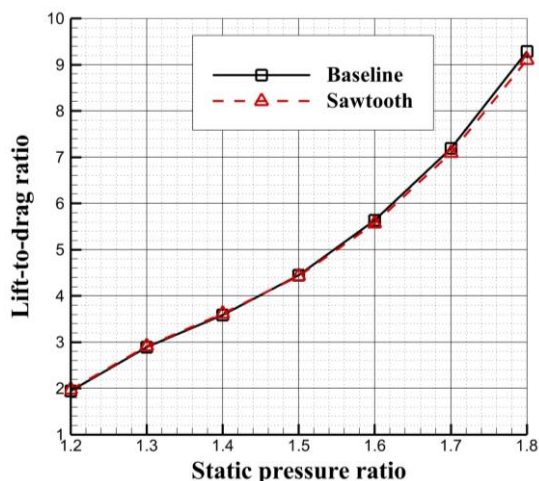


Fig. 15 Variation in the lift-drag ratio with the static pressure ratio

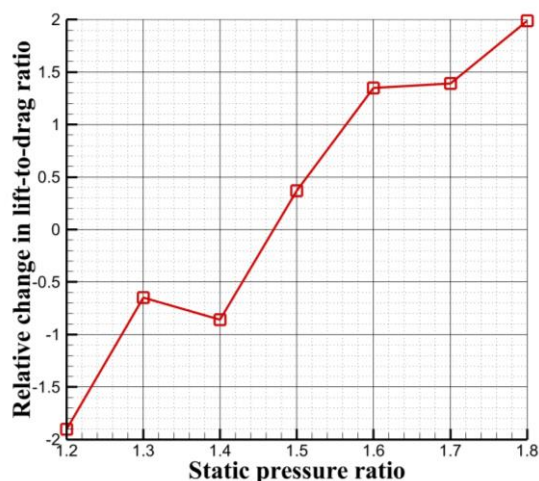


Fig. 16 Relative change in the lift-drag ratio as a function of static pressure ratio

Table 4 The data about total pressure loss coefficient and relative change in total pressure loss coefficient with respect to Mach number

Mach number	Baseling total pressure loss coefficient	Sawtooth total pressure loss coefficient	Relative change in total pressure loss coefficient
0.7	0.0253	0.0374	-47.83%
0.9	0.0446	0.0375	16.02%
1.2	0.1646	0.1671	-1.54%
1.35	0.1913	0.1822	4.76%
1.5	0.1663	0.1742	-4.77%
1.7	0.1439	0.1433	0.43%

is defined in Equation (3), and its value under different static pressure ratios is shown in Fig. 16. The lift-drag ratio of the baseline cascade and the leading-edge sawtooth cascade, as well as the relative change rate of their lift-drag ratio with respect to the static pressure ratio, are depicted in Table 3.

$$\text{Relative variation} = \frac{L/D_1 - L/D_2}{L/D_1} \times 100\% \quad (3)$$

where  $L/D_1$  and  $L/D_2$  are the lift-drag ratios of the baseline and leading-edge sawtooth cascades, respectively.

It can be seen in Fig. 15 that when the static pressure ratio is less than 1.5, the lift-drag ratio of the leading-edge sawtooth cascade is higher than that of the baseline cascade, but when the static pressure ratio is greater than or equal to 1.5, the lift-drag ratio of the leading-edge sawtooth cascade is lower. Further, it is clear from Fig. 16 that the relative change in the lift-drag ratio increases with the increase in the static pressure ratio.

Integrating the trends observed in Fig. 15 and Fig. 16 with the data from Table 3, it is noted that at static pressure ratio  $p_2/p_1=1.2$ , the lift-drag ratio ( $L/D$ ) for the baseline cascade is 1.9406, whereas for the leading-edge sawtooth cascade, it is 1.9775, resulting in a relative change of -1.9%. At static pressure ratio  $p_2/p_1=1.3$ , the lift-drag ratio for the baseline cascade is 2.8934, and for the leading-edge sawtooth cascade, it is 2.9123, with a relative change of -0.65%. At static pressure ratio  $p_2/p_1=1.4$ , the lift-drag ratio for the baseline cascade is 3.5828, and for the leading-edge sawtooth cascade, it is 3.6135, leading to a relative change of -0.86%. When static pressure ratio  $p_2/p_1$  increases to 1.5,

the lift-drag ratio for the baseline cascade is 4.4439, and for the leading-edge sawtooth cascade, it is 4.4275, with a minimal relative change of 0.3684%. At static pressure ratio  $p_2/p_1=1.6$ , the lift-drag ratio for the baseline cascade is 5.6393, and for the leading-edge sawtooth cascade, it is 5.5630, corresponding to a relative change of 1.35%. At static pressure ratio  $p_2/p_1=1.7$ , the lift-drag ratio for the baseline cascade is 7.1951, and for the leading-edge sawtooth cascade, it is 7.0950, with a relative change of 1.39%. Finally, at static pressure ratio  $p_2/p_1=1.8$ , the lift-drag ratio for the baseline cascade is 9.2880, and for the leading-edge sawtooth cascade, it is 9.1028, with a relative change of 1.99%. The lift-drag ratio for both the baseline cascade and the leading-edge sawtooth cascade increases with the augmentation of the static pressure ratio.

#### 4.2 Effect of Mach Number on the Performance of Leading-edge Sawtooth Cascade

In the previous section, the variation trends of the total pressure loss coefficient and lift-drag ratio of the baseline and leading-edge sawtooth cascades as a function of the static pressure ratio were obtained. However, these trends are still not sufficient to explain the advantages/disadvantages of the leading-edge sawtooth cascade over the baseline cascade, which are therefore examined in this section in terms of the effect of Mach number on the total pressure loss coefficient and lift-drag ratio of the two cascades.

##### (1) Variation of Total Pressure Loss Coefficient

The corresponding total pressure loss coefficients of both types of cascade are depicted in Fig. 17, the relative change in total pressure loss coefficient are presented in

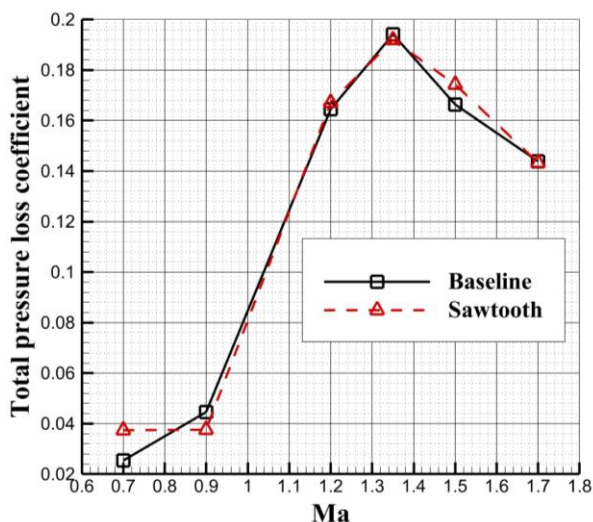


Fig. 17 Variation in the total pressure loss coefficient with the Mach number

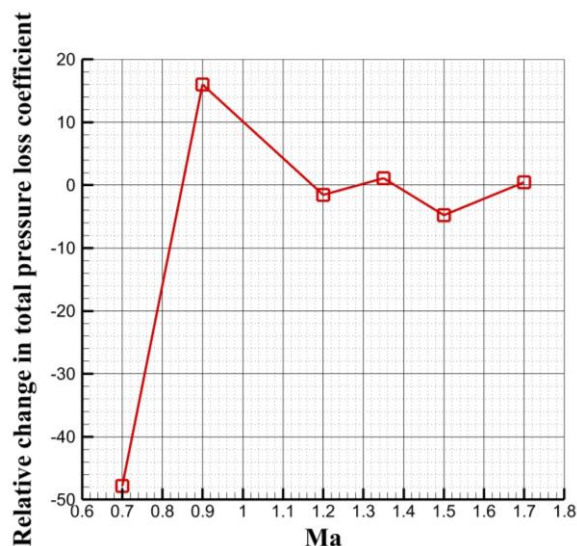


Fig. 18 Relative change in the total pressure loss coefficient as a function of the Mach number

Table 5 The data about lift-drag ratio and relative change in lift-drag ratio with respect to Mach number

Mach number	Baseling lift-drag ratio	Sawtooth lift-drag ratio	Relative change in lift-drag ratio
0.7	25.4262	19.3551	23.8773%
0.9	20.2303	17.1915	15.0210%
1.2	5.5045	5.1873	5.7615%
1.35	4.4439	4.4275	0.3684%
1.5	4.7760	4.5707	4.2988%
1.7	4.0303	3.9256	2.5986%

Fig. 18. The total pressure loss coefficients of the baseline cascade and the leading-edge sawtooth cascade, as well as the relative change rate of their total pressure loss coefficients with respect to the Mach number, are depicted in Table 4.

To investigate the effect of Mach number on the total pressure loss coefficient, the Mach number range of 0.7-1.7 is considered, which spans subsonic to supersonic speeds. The relevant results for the total pressure loss coefficient are presented in Fig. 17. To quantify the disparity between the baseline and leading-edge sawtooth cascades, the concept of relative variation in the total pressure loss coefficient is applied, as defined in Equation (2), and the corresponding data are depicted in Fig. 18. It can be seen that the total pressure loss coefficient progressively rises as the Mach number increases from 0.7 to 1.35, with a slow ascent between 0.7 and 0.9, a more rapid increase between 0.9 and 1.35, and a subsequent gradual decline up to 1.7. Integrating the trends observed in Fig. 17 and Fig. 18 with the data from Table 4, it is noted that at Ma=0.7, the total pressure loss coefficient for the baseline cascade is 0.0253, whereas for the leading-edge sawtooth cascade, it is 0.0374, resulting in a relative change of -47.83%. At Ma = 0.9, the total pressure loss coefficient for the baseline cascade is 0.0446, and for the leading-edge sawtooth cascade, it is 0.0357, with a relative change of 16.02%. At Ma = 1.2, the total pressure loss coefficient for the baseline cascade is 0.1646, and for the leading-edge sawtooth cascade, it is 0.1671, leading to a relative change of -1.54%. When the Mach number increases to 1.35, the total pressure loss coefficient for the baseline cascade is 0.1913, and for the leading-edge

sawtooth cascade, it is 0.1822, with a relative change of 4.76%. At Ma = 1.5, the total pressure loss coefficient for the baseline cascade is 0.1663, and for the leading-edge sawtooth cascade, it is 0.1742, corresponding to a relative change of -4.77%. Finally, at Ma = 1.7, the total pressure loss coefficient for the baseline cascade is 0.1439, and for the leading-edge sawtooth cascade, it is 0.1477, with a relative change of 0.43%.

(2) Variation in the Lift-Drag Ratio

In this section, the influence of the variation in the Mach number (0.7-1.7) on the lift-drag ratio is investigated. The relevant results are shown in Fig. 19. To quantify the improvement or deterioration in the lift-drag ratio of the leading-edge sawtooth cascade with respect to that of the baseline cascade, the relative variation in the lift-drag ratio is used, which is defined in Equation (3). The relevant results are shown in Fig. 20. The lift-drag ratio of the baseline cascade and the leading-edge sawtooth cascade, as well as the relative change rate of their lift-drag ratio with respect to the static pressure ratio, are depicted in Table 5. It can be seen in Fig. 19 that the lift-drag ratio of the baseline cascade is larger than that of the leading-edge sawtooth cascade when the Mach number is in the range of 0.7-1.7. According to Fig. 20, the lift-drag ratio of both the cascades decreases with the increase in the Mach number from 0.7 to 1.35, increases with the increase in Mach number from 1.35 to 1.5, and then again decreases with the increase in Mach number from 1.5 to 1.7. Integrating the trends observed in Fig. 19 and Fig. 20 with the data from Table 5, it is noted that at Ma=0.7, the lift-drag ratio (L/D) for the baseline cascade is 25.4262, whereas for the

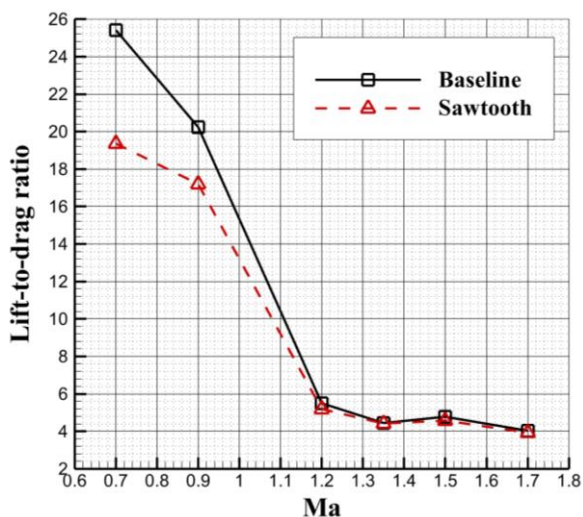


Fig. 19 Variation in the lift-drag ratio with the Mach number

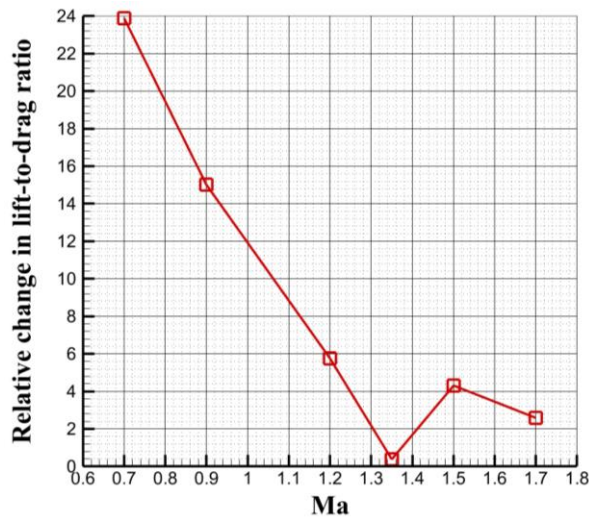


Fig. 20 Relative change in the lift-drag ratio as a function of the Mach number

Table 6 The data about total pressure loss coefficient and relative change in total pressure loss coefficient

Baseline total pressure loss coefficient	Sawtooth total pressure loss coefficient	Relative change in total pressure loss coefficient
0.191257	0.18216	4.76%

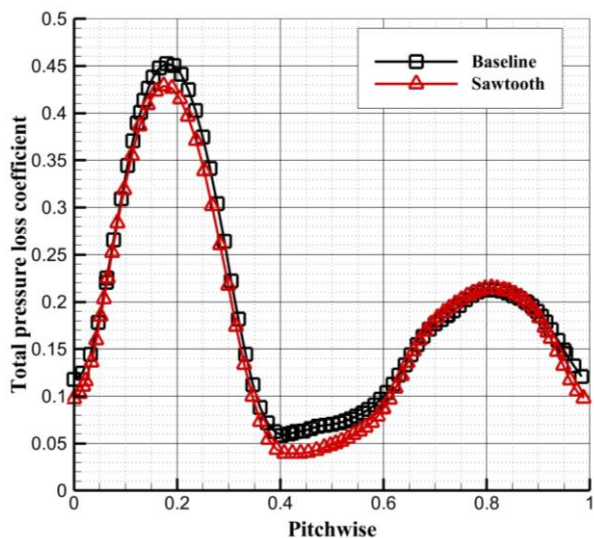


Fig. 21 Variation in the total pressure loss coefficients of the leading-edge sawtooth cascade and baseline cascade along the pitch direction

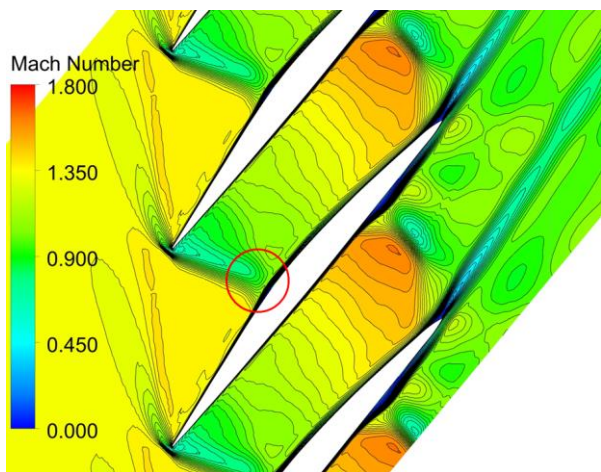
leading-edge sawtooth cascade, it is 19.3551, resulting in a relative change of 23.8773%. At  $Ma = 0.9$ , the lift-drag ratio for the baseline cascade is 20.2303, and for the leading-edge sawtooth cascade, it is 17.1915, with a relative change of 15.0210%. At  $Ma = 1.2$ , the lift-drag ratio for the baseline cascade is 5.5045, and for the leading-edge sawtooth cascade, it is 5.1873, leading to a relative change of 5.7615%. When the Mach number increases to 1.35, the lift-drag ratio for the baseline cascade is 4.4439, and for the leading-edge sawtooth cascade, it is 4.4275, with a minimal relative change of 0.3684%. At  $Ma = 1.5$ , the lift-drag ratio for the baseline cascade is 4.7760, and for the leading-edge sawtooth cascade, it is 4.5707, corresponding to a relative change of 4.2988%. Finally, at  $Ma = 1.7$ , the lift-drag ratio for the baseline cascade is

4.0303, and for the leading-edge sawtooth cascade, it is 3.9256, with a relative change of 2.5986%. Despite the overall decrease in lift-drag ratio with increasing Mach numbers, the lift-drag ratio of the baseline cascade consistently surpasses that of the leading-edge sawtooth cascade.

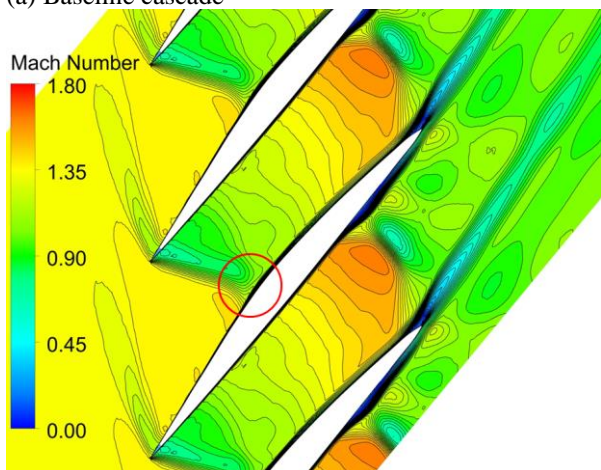
### 4.3 Influence of Leading-edge Sawtooth Structure on the Flow Field in the Cascade Passage

Until now, the effects of static pressure ratio and Mach number on the aerodynamic performance of leading-edge sawtooth cascades have been examined. In this section, the influence of leading-edge sawtooth structure on the flow field in the cascade channel is studied at a Mach number  $Ma$  of 1.35 and static pressure ratio  $p_2/p_1$  of 1.5. Specifically, the total pressure loss coefficient, Mach number cloud map, and total pressure loss coefficient cloud map of the leading-edge sawtooth and baseline cascades are analyzed, and their flow fields are compared. The variation in the total pressure loss coefficient of the two cascades with the grid number is shown in Fig. 6. The variation in the total pressure loss coefficient of the two cascades along the pitch direction is shown in Fig. 21. The total pressure loss coefficients of the baseline cascade and the leading-edge sawtooth cascade, as well as the relative change rate of their total pressure loss coefficients, are depicted in Table 6. It is clear from Fig. 6 and Table 6 that when the total pressure loss coefficient is not affected by the number of grids, the average total pressure loss coefficient of the leading-edge sawtooth cascade is  $\zeta = 0.18216$  and that of the baseline cascade is  $\zeta = 0.191257$ , which corresponded to a reduction of 4.76%.

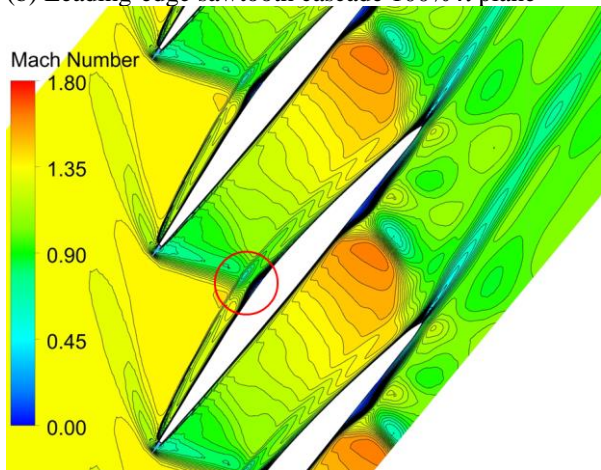
The Mach number distribution is used to reflect the flow characteristics of the fluid passing through the leading-edge sawtooth structure. A two-dimensional plane is selected for the analysis. To examine the difference of the flow field between the tooth tip and the tooth root of



(a) Baseline cascade



(b) Leading-edge sawtooth cascade 100%  $\lambda$  plane

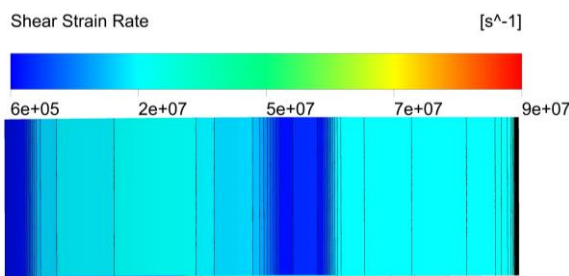


(c) Leading-edge sawtooth cascade 50%  $\lambda$  plane

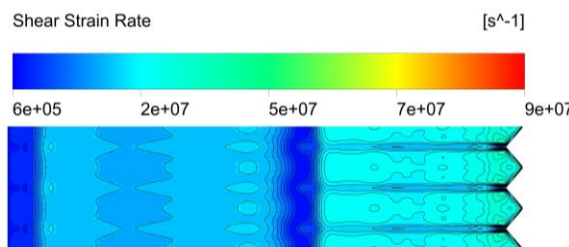
**Fig. 22 Mach number distribution of baseline cascade and leading-edge sawtooth cascade**

the leading-edge sawtooth cascade, the cloud map of Mach number distribution is obtained. The Mach number distribution cloud map of the baseline cascade is shown in Fig. 22(a), while that of 50% of spanwise height ( $\lambda$ ) and 100%  $\lambda$  planes of the leading-edge sawtooth cascade is shown in Fig. 22(b) and Fig. 22(c), respectively. Figure 24 shows the flow vortex generated by the leading-edge sawtooth cascade at the suction surface.

When a channel shock wave is incident on the suction side at 30% of the chord (30%  $c$ ), it leads to flow separation due to the shock wave/boundary layer interaction. On the



(a) Baseline cascade



(b) Leading-edge sawtooth cascade

**Fig. 23 Shear strain rate cloud map of baseline cascade and leading-edge sawtooth cascade**

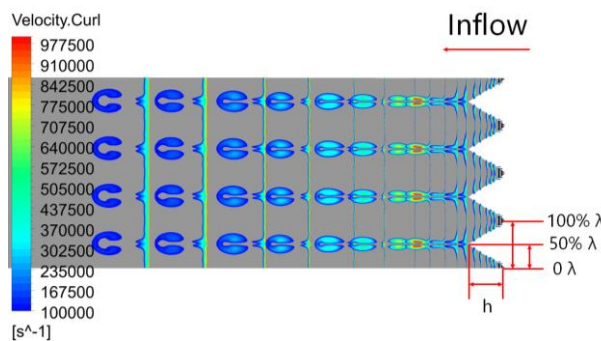


**Fig. 24 Streamwise vortex development process**

pressure side, the shock wave impinges at 60% $c$ , causing flow separation as well, as shown in Fig. 33(a). Comparing Figs. 22(a), 22(b), and 22(c), it can be observed that the low-speed flow area on the suction side (30%  $c$ ) of the leading-edge sawtooth cascade at 50%  $\lambda$  is larger than that at 100%  $\lambda$  spanwise height and that of the baseline cascade. The wake low-speed area width is also narrower than that at 100%  $\lambda$ . It is evident from Figs. 23(a) and 23(b) that the blue streaks at the root of the leading-edge sawtooth cascade (at 50%  $\lambda$ ) are caused by streamwise vortices, which result in a lower shear strain rate at the streak location compared to the sides of the streak. A low wall shear rate also implies that the fluid detaches from the wall. Combining the development process of the streamwise vortices shown in Fig. 24, it can be observed that the incoming gas at 100%  $\lambda$  of the leading-edge sawtooth cascade flows towards the 50%  $\lambda$  and generates streamwise vortices at 50%  $\lambda$  spanwise height, which then detach from the suction surface of the blade and develop in the streamwise direction. At the same time, according to Figs. 22(b) and 22(c), at 50%  $\lambda$  of the leading-edge sawtooth cascade, the Mach number in the near-wall area, after passing the 40% $c$  position on the suction surface, is higher than that at the 100%  $\lambda$ . The base area at the trailing edge is lower than that at the 100%  $\lambda$  spanwise height and that of the baseline cascade. Moreover, as shown in Fig. 18, the wake area of the leading-edge sawtooth cascade is smaller than that of the baseline cascade, which can be attributed

to the decrease in the deviation angle. Comparing Figs. 23(a) and 23(b), it can be seen that the deviation angle of the leading-edge sawtooth cascade is reduced, the width of the wake low-speed area is decreased, and the leading-edge sawtooth structure reduces the flow separation at the trailing edge under 50%  $\lambda$  spanwise height, thereby reducing the total pressure loss in the wake. Xu et al. (2023), Chen et al. (2016) and Duan et al. (2023) reported that the induced streamwise vortices can effectively suppress the separation at the trailing-edge, which in turn reduces the separation loss. However, the leading-edge sawtooth structure intensifies the shock wave/boundary layer interaction on the suction side at 50%  $\lambda$ , causing flow separation at 30%  $c$  position on the suction surface of the airfoil to intensify, resulting in a separation bubble behind the shock on the suction side, as indicated by the red circle in Fig. 22(c).

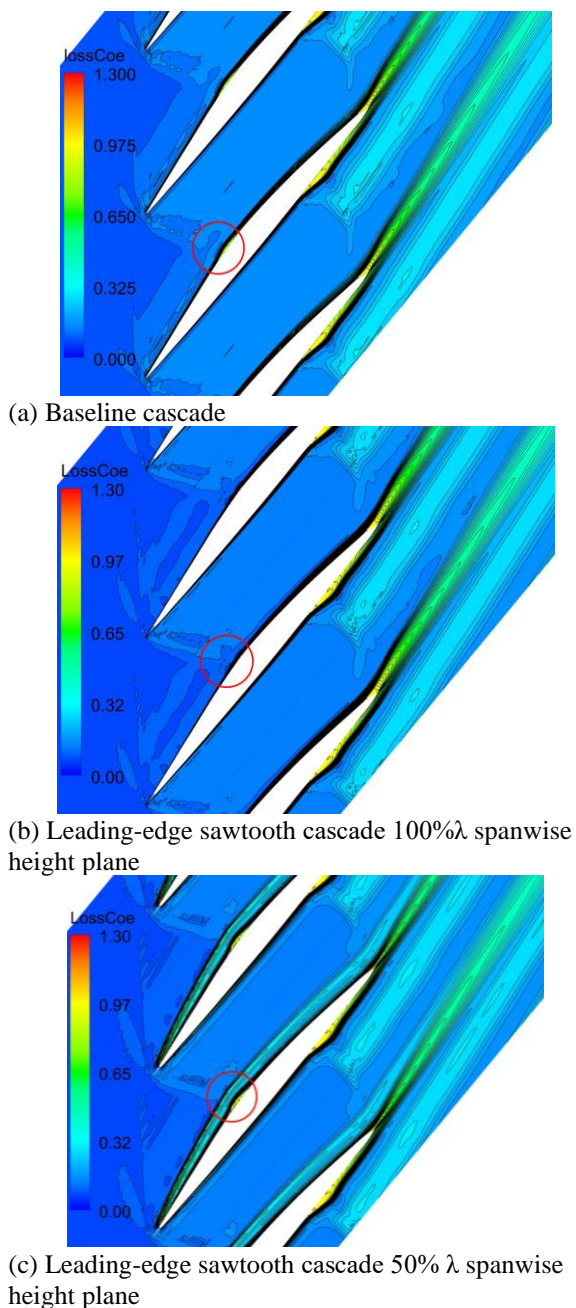


**Fig. 25 Total pressure loss coefficients of baseline cascade and leading-edge sawtooth cascade**

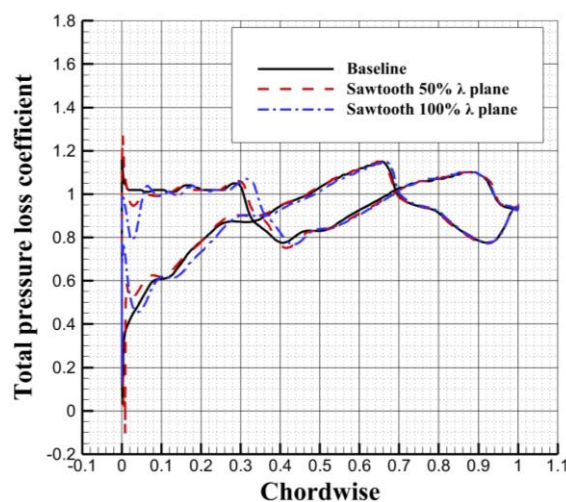


**Fig. 26 Total pressure loss coefficients of baseline cascade and leading-edge sawtooth cascade**

To further understand the influence of the leading-edge sawtooth structure on the flow field, the total pressure loss coefficient distribution of the two types of cascade is analyzed. The distributions of the total pressure loss coefficient of the baseline cascade and that of the leading-edge sawtooth cascade at 100%  $\lambda$  spanwise height plane and 50%  $\lambda$  planes are shown in Figs. 25(a), 25(b), and 25(c), respectively.

Comparing Fig. 25(a) to Fig. 25(c), it is evident that the distribution of the total pressure loss coefficient at the 50%  $\lambda$  of the leading-edge sawtooth cascade markedly differs from that of both the baseline cascade and the leading-edge sawtooth cascade at 100%  $\lambda$ . The distribution of the incoming flow's total pressure loss coefficient is also distinct from that of the baseline cascade and the leading-edge sawtooth cascade at 100% $\lambda$ . The total pressure loss coefficient in the area between the flow vortex and the suction surface wall is higher than that at the same position within the baseline cascade channel and the leading-edge sawtooth cascade at 100%  $\lambda$ . As previously analyzed, the induction of a flow vortex on the suction surface side at the 50%  $\lambda$  of the leading-edge sawtooth cascade leads to an increased mixing loss between the flow vortex and the blade's suction surface, resulting in a higher total pressure loss in this region. However, the flow vortex enhances the flow field's resistance to separation, reduces the wake deflection angle, and effectively improves the wake shape of the blade, thereby reducing the wake loss.

Upon examining Fig. 26, it is evident that the total pressure loss at the leading edge of the baseline cascade slightly exceeds that of the leading-edge sawtooth cascade at the 50%  $\lambda$ . Furthermore, the position of the channel shock wave for the leading-edge sawtooth cascade at 50%  $\lambda$  is situated further aft compared to the baseline cascade. The channel shock wave in the baseline cascade is located at approximately the 29.5% chord length position, while for the leading-edge sawtooth cascade at 50%  $\lambda$ , the shock is observed at the 30% chord length position. Additionally, the total pressure loss coefficient at the leading edge of the leading-edge sawtooth cascade at 100%  $\lambda$  is less than that of both the baseline cascade and the leading-edge sawtooth cascade at 50%  $\lambda$ , with the channel shock wave appearing at a 31%  $c$  position. These observations are in alignment with the analysis of the leading edge and channel shock wave positions depicted in Fig. 25.

Based on the above analysis, the flow field characteristics of the leading-edge sawtooth and baseline cascades have the following similarities:

- (1) The distribution trend of total pressure loss coefficient is almost the same.
- (2) The flow field distributions of the two are roughly the same.

In addition, the flow field characteristics of the two cascades have the following differences:

- (1) The total pressure loss coefficient of the leading-edge sawtooth cascade is generally lower than that of the baseline cascade.
- (2) The variation rate at the local position in the two total pressure loss coefficient distribution maps is different.
- (3) The leading-edge sawtooth cascade forms a flow vortex at 50%  $\lambda$ , which has stronger anti-separation ability than the baseline cascade, i.e., it reduces the flow separation at the suction surface of the blade as well as the lag angle, so the wake loss is also reduced.

#### 4.4 Effect of Leading-edge Sawtooth Structure on the Blade Surface Flow

##### (1) Static Pressure Coefficient

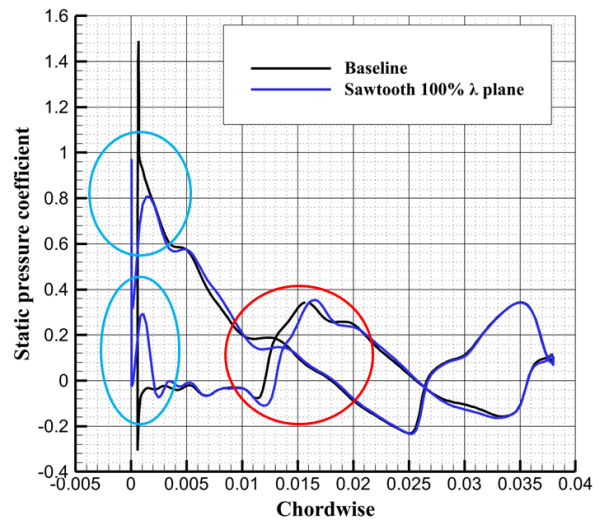
In the previous section, the flow field characteristics of the leading-edge sawtooth and baseline cascades were compared. However, the flow field analysis is not enough to evaluate the performance of the leading-edge sawtooth cascade. Thus, the static pressure coefficient is now analyzed. To quantify the blade surface load, the flow field of the two cascades is examined, and the influence of sawtooth structure on the blade surface load is investigated. Further, the static pressure coefficient is used to describe the blade surface load, which is defined as follows:

$$C_p = \frac{p - p_{in}}{\frac{1}{2} \rho_{in} v_{in}^2} \quad (4)$$

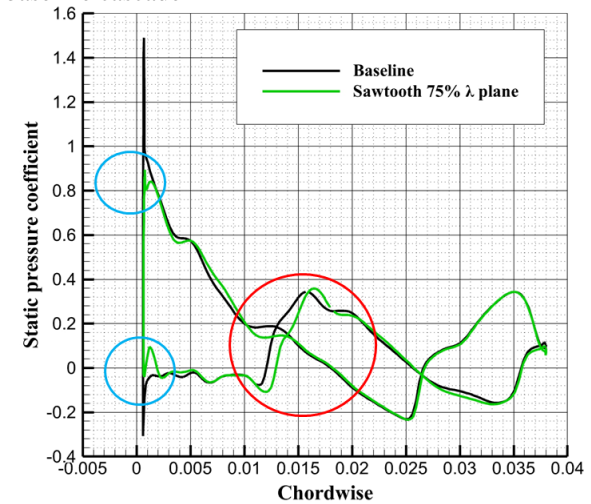
where  $p$  is the static pressure at the blade surface,  $p_{in}$  is the static pressure at the inlet of the blade, and  $v_{in}$  is the velocity at the inlet of the blade.

To comprehensively analyze the effect of sawtooth structure on the static pressure coefficient of the two cascade gratings, the static pressure coefficients for 100%  $\lambda$ , 75%  $\lambda$ , and 50%  $\lambda$  of the leading-edge sawtooth cascade grating are compared with the that of the baseline blade cascade. The results are shown in Figs. 27(a), 27(b), and 27(c), respectively.

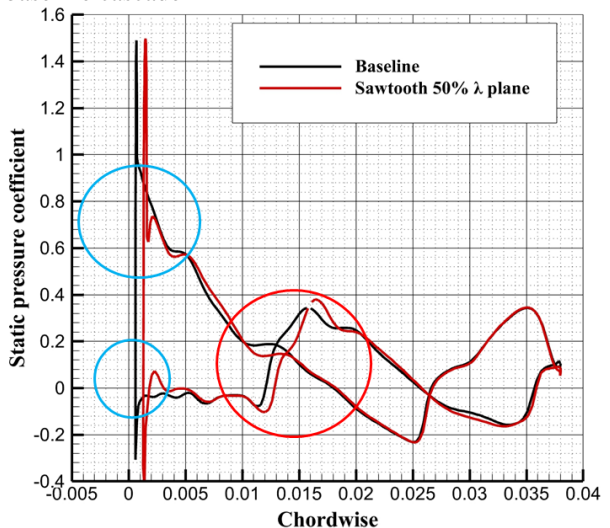
Analogous to the diffusion factor  $D$ , Goodhand & Miller (2011) proposed the factor  $D_{spike}$  for evaluating the strength of leading-edge spike, which is defined in Equation (5). Liu et al. (2013) and Kong (2020) argued that the presence of leading-edge spike can cause a drastic change in the velocity gradient of the leading-edge of the leaf pattern, leading to the rapid thickening of the attached surface layer or even early turning, thereby increasing the leaf pattern loss.



(a) Leading-edge sawtooth cascade 100%  $\lambda$  plane vs. baseline cascade



(b) Leading-edge sawtooth cascade 75%  $\lambda$  plane vs. baseline cascade



(c) Leading-edge sawtooth cascade 50%  $\lambda$  plane vs. baseline cascade

**Fig. 27** Distribution of static pressure coefficients in each plane of the leading-edge sawtooth cascade and the baseline cascade along the chord direction

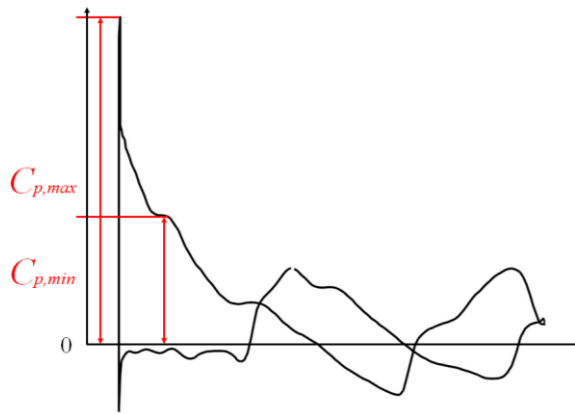


**Fig. 28 Definition of maximum and minimum static pressure coefficients**

**Table 7 The data about the leading-edge spike evaluation factor**

Cascade	Spanwise	$D'_{spike}$	The average of $D'_{spike}$	The relative change of $D'_{spike}$
Baseline	Any spanwise	0.6072	0.6072	27.68%
Sawtooth	50% $\lambda$	0.6208	0.4391	
	75% $\lambda$	0.3692		
	100% $\lambda$	0.4182		

$$D'_{spike} = \frac{u_{max} - u_{min}}{u_{max}} \quad (5)$$

The above parameters are evaluated using the isentropic Mach number for the leading-edge spike. Here, the static pressure coefficient is used to determine the leading-edge spike strength, which is defined in terms of the leading-edge spike evaluation factor, as shown in Equation (6), and the relevant definitions are provided in Fig. 28. The data about the leading-edge spike evaluation factor is shown in Table 7.

$$D'_{spike} = \frac{C_{p,max} - C_{p,min}}{C_{p,max}} \quad (6)$$

As shown in Fig. 29 and Table 7,  $D'_{spike} = 0.6072$  for the baseline blade,  $D'_{spike} = 0.4182$  for the leading-edge sawtooth blade at 100%  $\lambda$ ,  $D'_{spike} = 0.3692$  for the leading-edge sawtooth blade at 75%  $\lambda$ ,  $D'_{spike} = 0.6208$  for the leading-edge sawtooth blade at 50%  $\lambda$ , and the arithmetic average of  $D'_{spike}$  for the leading-edge sawtooth blade = 0.4391. Typically, the smaller the  $D'_{spike}$ , the lower the total pressure loss.

Based on the comparison of the static pressure coefficients (Fig. 27) and  $D'_{spike}$  (Fig. 29) between the leading-edge sawtooth and baseline blades, and the data of Table 7, it can be seen that the static pressure coefficients of the two blades are approximately the same. The blue circles in the figure show that the  $D'_{spike}$  of the leading-edge sawtooth grating at 100%  $\lambda$  and 75%  $\lambda$  are reduced by 33.13% and 39.20%, respectively, compared with that of the baseline grating, and that of the leading-edge sawtooth grating at 50%  $\lambda$  is basically the same as that of the baseline

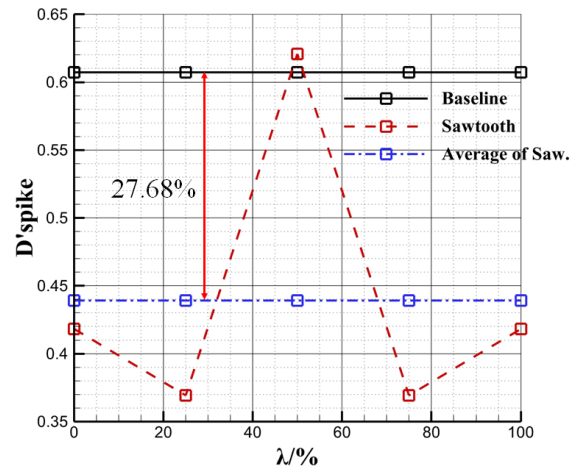


**Fig. 29 Calculated values of  $D'_{spike}$**

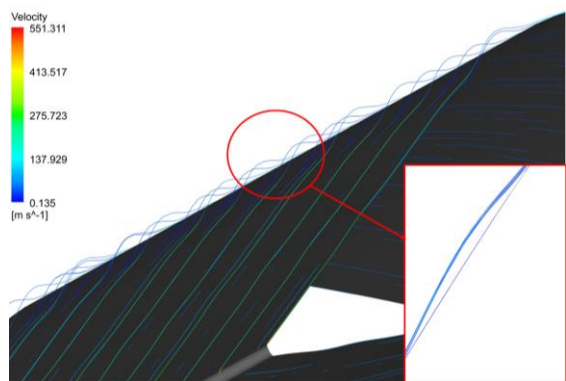
grating. Further, the average  $D'_{spike}$  of the entire sawtooth structure is reduced by 27.68% with respect to that of the baseline grating. Thus, the sawtooth structure can reduce the load of the blade in the leading-edge region.

The gradient of static pressure coefficient at the three heights of the leading-edge sawtooth blade cascade (shown by red circle in Fig. 25) is larger than that of the baseline blade cascade, and the location of excitation wave generation in the channel is shifted backward. Thus, the leading-edge sawtooth structure strengthens the excitation intensity in the channel of the blade grating.

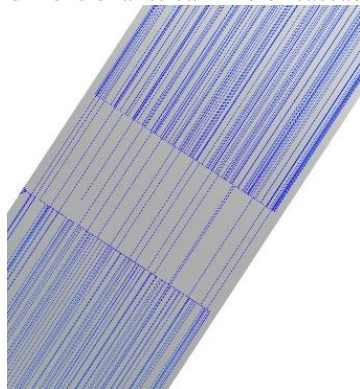
## (2) Wall Flow Spectrum

In this section, the variation in the flow spectrum on the suction surface is derived using topological analysis, and the results are shown in Fig. 30 and Fig. 31. Figures 30(a) and 30(b) demonstrate the near-wall 3D flow lines and wall flow lines for the baseline blade cascade, respectively, which indicate that at 35% $c$  of the suction surface, the fluid undergoes segregation and re-attaches to the suction surface at 40% $c$ . Figure 31(a) and Fig. 31(b) show the near-wall 3D flow lines and wall flow lines of the leading-edge sawtooth blade cascade, respectively, where closed separation bubbles are generated on the suction surface around 30% $c$  to 40% $c$ . Further, the flow separation is more drastic as compared to that of the baseline blade cascade. The difference between the flow spectra of the two cascades may be attributed to the fact that the increased intensity of the excitation wave in the channel on the suction surface side enhances the excitation-boundary layer interference on the suction surface at 30% $c$  to 40% $c$ , which results in the formation of closed separation bubbles at the suction surface as well as a sharp increase in the losses (Tong et al., 1992; Zhang, 2007). The presence of separation bubble structure in this flow field can also be verified in the Mach number cloud map (Fig. 22), the total pressure loss coefficient cloud map (Fig. 25), and the static pressure coefficient distribution curve (Fig. 27).

In summary, the leading-edge spike coefficient at 100%  $\lambda$  and 75% $\lambda$  of the sawtooth blade cascade are reduced by 33.13% and 39.20%, respectively, with respect to that of the baseline blade cascade, while the leading-edge spike coefficient at 50%  $\lambda$  of sawtooth blade cascade is basically the same as that of the baseline blade cascade. Further, the average leading-edge spike coefficient of the

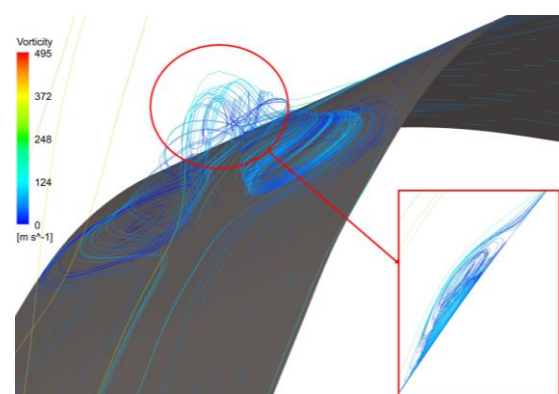


(a) Three-dimensional streamline of cascade channel

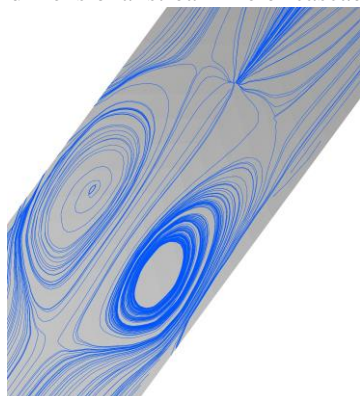


(b) Streamline of the blade surface

**Fig. 30 Streamline of baseline cascade**



(a) Three-dimensional streamline of cascade channel



(b) Streamline of the blade surface

**Fig. 31 Streamline of leading-edge sawtooth cascade**

entire sawtooth structure is reduced by 27.68%. Thus, it is clear that the leading-edge sawtooth structure can effectively reduce the leading-edge spike and the

corresponding total pressure loss. However, it can exacerbate the excitation-boundary layer interference on the suction surface, enhance and push back the excitation wave in the suction surface channel, and form the suction surface separation bubble.

## 5. CONCLUSION

In this study, the advantages and disadvantages of the leading-edge sawtooth blade cascade over the baseline blade cascade were established by comparing their performances under three operating conditions: fixed Mach number and variable static pressure ratio, fixed static pressure ratio and variable Mach number, and fixed static pressure ratio and fixed Mach number. The main findings are summarized as follows:

(1) At a Mach number of 1.35 and static pressure ratios between 1.2 and 1.8, the leading-edge sawtooth blade cascade consistently exhibited a lower total pressure loss coefficient compared to the baseline blade cascade. Additionally, the lift-drag ratio for the leading-edge sawtooth blade cascade surpassed that of the baseline when the static pressure ratio was less than or equal to 1.4, but fell below it when the ratio exceeded 1.5.

(2) Across a Mach number range of 0.7 to 1.7 with a static pressure ratio of 1.5, both the baseline and leading-edge sawtooth blades reached their peak total pressure loss coefficient at a Mach number of 1.35. Here, the lift-drag ratio for the leading-edge sawtooth blade was found to be lower than the baseline.

(3) Comparative analysis at a Mach number of 1.35 and a static pressure ratio of 1.5 revealed that the leading-edge sawtooth structure generated a flow vortex at 50% spanwise height ( $\lambda$ ), which enhanced the anti-separation capabilities and reduced the deflection angle. The average total pressure loss coefficient for the baseline blade was 0.191257, whereas for the leading-edge sawtooth blade, it was 0.18216, indicating a 4.76% reduction.

(4) The leading-edge sawtooth significantly reduced the leading-edge spike and the associated total pressure loss, with the average leading-edge spike evaluation factor decreasing by 27.68% compared to the baseline blade. However, this design also intensified the excitation-boundary layer interaction on the suction surface, leading to the formation of a separation bubble and a shift in the excitation wave position to the rear at 40%  $c$  in suction surface.

## ACKNOWLEDGEMENTS

The research was supported by the National Natural Science Foundation of China (52106045), Shenzhen Key Project of Basic Research (JCYJ20200109141403840) and Shenzhen Key Laboratory Preparation Start-up Project (ZDSYS20220527171405012).

## REFERENCES

Chen, M., (2017). *Research on the effect of serrated trailing edge of stator on a low speed axial compressor* [Master, Nanjing University of Aeronautics and Astronautics]. Nanjing.

Chen, M., Li, C., Shao, X., & Yan, Z., (2018). Numerical

- simulation on the effect of serrated trailing edge on the compressor cascade. *Journal of Chongqing University of Technology (Natural Science)*, 32(7), 83-93. [http://doi.org/10.3969/j.issn.1674-8425\(z\).2018.07.013](http://doi.org/10.3969/j.issn.1674-8425(z).2018.07.013)
- Chen, W., Qiao, W., Duan, W., & Wei, Z. (2021). Experimental study of airfoil instability noise with wavy leading edges. *Applied Acoustics*, 172, 107671.
- Chen, W., Qiao, W., Tong, F., Duan, W., & Liu, T. (2016). Effect of leading-edge serrations on boundary layer instability noise. *Acta Aeronautica et Astronautica Sinica*, 37(12), 3634-3645. <http://doi.org/10.7527/S1000-6893.2016.0104>
- Duan, W., Chen, W., Zhao, X., & Qiao, W. (2023). Numerical studies on the effect of leading edge tubercles on a low-pressure turbine cascade. *Energies*, 16(11), 4398. <http://doi.org/10.3390/en16114398>
- Goodhand, M. N., & Miller, R. J. (2011). Compressor leading edge spikes: a new performance criterion. *Journal of Turbomachinery*, 133(2). <http://doi.org/10.1115/1.4000567>
- He, Y., Li, X., Feng, H., Jiang, L., & Qu, W. (2019a). Effect of saw tooth structure on wake characteristics of compressor blades. *Mechanical Science and Technology for Aerospace Engineering*, 38(8), 1301-1306. <https://doi.org/10.13433/j.cnki.1003-8728.20180313>
- He, Y., Li, X., Feng, H., Jiang, L., & Qu, W. (2019b). Effect of serrated trailing edge on blade wake characteristics. *Mechanical Engineering & Automation*, (1), 15-20. <https://link.cnki.net/urlid/14.1319.TH.20190219.1643.012>
- Hu, H. (2020). *Influence of leading edge sawtooth on aerodynamic and noise performance of forward-flying multi-rotor rotors*. 2020 Annual Online Symposium of the Acoustics Division of the Chinese Aeronautical Society, China Beijing. <http://doi.org/10.26914/c.cnkihy.2020.017612>
- Kondo, H., Sakaguchi, H., Hachiyama, M., & Takamori, S. (1968). *Notes on the suitable configuration for supersonic cascade tunnel*. Japan National Aerospace Laboratory: Ibaraki-ken.
- Kong, X. (2020). *Design of the high subsonic profiles with wide range and low loss* [Master, Nanjing University of Aeronautics and Astronautics]. Nanjing.
- Liang, D., Li, Y., Zhou, Z., Wiśniewski, P., & Dykas, S. (2021). Structure and topology analysis of separated vortex in forward-swept blade. *Frontiers in Energy Research*, 9, 693596. <http://doi.org/10.3389/fenrg.2021.693596>
- Liu, B., Yuan, C., & Yu, X. (2013). Effects of leading-edge geometry on aerodynamic performance in controlled diffusion airfoil. *Journal of Propulsion Technology*, 34(7), 890-897. <http://doi.org/10.13675/j.cnki.tjjs.2013.07.006>
- Liu, X., Zang, B., & Azarpeyvand, M. (2022). Wake-aerofoil interaction noise control with trailing-edge serrations. *Experimental Thermal and Fluid Science*, 130, 110510. <http://doi.org/https://doi.org/10.1016/j.expthermflusci.2021.110510>
- Menter, F. R., Kuntz, M., & Langtry, R. (2003). Ten years of industrial experience with the SST turbulence model. *Turbulence, Heat and Mass Transfer*, 4(1), 625-632. Begell House.
- Sun, G., Chen, E., & Yang, A. (2021). Numerical study on the flow separation controlling by sawtooth leading edge of the blade. *Energy Research and Information*, 37(4), 229-237. <http://doi.org/10.13259/j.cnki.eri.2021.04.007>
- Tong, B., Zhang, B., & Cui, E. (Eds.). (1992). *Non-constant flow and vortex motion*. Defence Industry Press.
- Wang, L. (2019). *Effect of serrated trailing edge on aerodynamic performance of high-load compressor cascade* [Doctor, Dalian Maritime University]. Dalian.
- Wang, Y. (2020). *Research on the effect of trailing edge serrated distribution of stator on high speed axial compressor* [Master, Nanjing University of Aeronautics and Astronautics]. Nanjing.
- Wu, W. (2016). *The aerodynamic research on the serrated trailing edge of blade* [Master, Nanjing University of Aeronautics and Astronautics]. Nanjing.
- Xu, W., Zou, S., Sun, D., Lu, W., Ren, G., & Zhao, H., (2023). Effect of suction leading edge vortex generator on characteristics of compressor cascade. *Journal of Aerospace Power*. <http://doi:10.13224/j.cnki.jasp.20230485>.
- Yang, Y., Liu, Y., Hu, H., Liu, X., Wang, Y., Arcondoulis, E. J. G., & Li, Z. (2020a). Experimental study on noise reduction of a wavy multi-copter rotor. *Applied Acoustics*, 165, 107311. <https://doi.org/10.1016/j.apacoust.2020.107311>
- Yang, Y., Wang, Y., Liu, Y., Hu, H., & Li, Z. (2020b). Noise reduction and aerodynamics of isolated multi-copter rotors with serrated trailing edges during forward flight. *Journal of Sound and Vibration*, 489, 115688. <https://doi.org/10.1016/j.jsv.2020.115688>
- Yin, S., Jin, D., Gui, X., & Zhu, F. (2010). Application and comparison of SST model in numerical simulation of the axial compressors. *Journal of Thermal Science*, 19(4), 300-309. <http://doi.org/10.1007/s11630-010-0387-8>
- Yu, Y. (2018). *Influence of the trailing edge serration on the aerodynamic performance of a high speed compressor cascade*. [Master, Harbin Institute of Technology]. Haerbin.
- Zhang, H. (2007). *Investigation on application of dihedral/swept blade and boundary layer suction to control vortex configurations in compressor cascades*. [Doctor, Harbin Institute of Technology]. Haerbin.
- Zou, R., Li, C., An, Z., Shang, C., & Xuan, B. (2021). Numerical simulation research on aerodynamic characteristics of sawtooth trailing edge blade. *Journal of Nanjing University of Aeronautics & Astronautics*, 53(4), 546-550. <http://doi.org/10.16356/j.1005-2615.2021.04.007>